Electronic Supplementary Information

Strong interfacial energetics between catalysts and current collectors in aqueous sodium-air batteries

Myung-Jin Baek,‡[a] Jieun Choi,‡[a] Tae-Ung Wi,[a] Hyeong Yong Lim,[a] Min Hoon Myung,[a] Chanoong Lim,[a] Jinsu Sung,[a] Jeong-Sun Park,[b] Ju Hyun Park,[a] Yul Hui Shim,[a] Jaehyun Park,[a] Seok Ju Kang,[a] Youngsik Kim,[a,b] So Youn Kim,[c] Sang Kyu Kwak,*[a] Hyun-Wook Lee*[a] and Dong Woog Lee*[a]

*Corresponding author, E-mail: skkwak@unist.ac.kr; hyunwooklee@unist.ac.kr;

dongwoog.lee@unist.ac.kr

[a]School of Energy & Chemical Engineering, UNIST (Ulsan National Institute of Science and Technology), Ulsan, 44919, Republic of Korea

*E-mail address: skkwak@unist.ac.kr; hyunwooklee@unist.ac.kr; dongwoog.lee@unist.ac.kr

[b]Energy Materials and Devices Lab, 4TOONE corporation, 50 UNIST-gil, Ulsan, 44919, Republic of Korea

[c]School of Chemical and Biological Engineering, Institute of Chemical Processes, Seoul National University (SNU), Seoul 08826, Republic of Korea

‡ Authors with equal contributions to this work

Synthesis of monomers and polymers

The synthetic routes for the monomers and polymers are shown in scheme 1. Dopamine-*m*-acrylamide (DMA)[1] and dibenzyl trithiocarbonate (reversible addition-fragmentation chain transfer polymerization material (RAFT))[2] were synthesized following previously reported methods.

Synthesis of N-(4-hydroxyphenethyl)methacrylamide (PMA)

Approximately 1.0 g (7.3 mmol) of tyramine was dissolved in 30 ml of degassed methanol and bubbled with Ar gas for 5 min. When tyramine was completely dissolved, it was cooled in an ice bath, and a solution of methacrylic anhydride (8.02 mmol) in THF (1:4 volume ratio) was added drop-wise. The reaction mixture was stirred at room temperature for 3 h. After completion, methanol was removed under reduced pressure. The crude product was poured into a 10% aqueous sodium chloride solution and extracted with ethyl acetate (AcOEt) two times. The combined organic phase was washed with water and dried with $MgSO_4$. The solution was concentrated under reduced pressure and recrystallization in hexane: AcOEt (9: 1) (Y = 68%).

^{1}H NMR (ppm, DMSO-d_6, 400 MHz, δ): **9.16 (s, 1H), 7.95 (t, 1H, 5.2Hz), 6.99 (d, 2H, 8.4Hz), 6.68 (d, 2H, 8.4Hz), 5.61 (m, 1H), 5.30 (m, 1H), 3.26 (m, 2H), 2.63 (t, 2H, 7.6Hz), 1.84 (s, 3H); ^{13}C NMR** (ppm, DMSO-d_6, 100 MHz, δ): **167.80, 156.07, 140.55, 130.03, 129.93, 119.21, 115.55, 41.37, 34.75, 19.12; Mass: exact mass 205.1, found 206.1 (Fig. S1, S2 (a)).**

Synthesis of N-(2-phenethyl)methacrylamide (BMA)

To a dry 100-ml two-neck flask, 2-phenylamine (2.0 g, 16.5 mmol) and degassed 30 ml of methanol were added. The mixture was degassed with argon for 5 min, and 2.3-ml triethylamine (16.5 mmol) was added. The mixture was cooled in an ice bath, and methacrylic anhydride (18.98 mmol) in THF (1:4 volume ratio) was added drop-wise. Then, the mixture was stirred at room temperature for 3 h. After completion, methanol was removed under reduced pressure. The crude product was extracted with

AcOEt. The organic layer was washed with 1 N HCl, brine, and dried with $MgSO_4$.The solution was concentrated under reduced pressure and purified with a flash column (Hexane: AcOEt = 5: 1) (Y = 65%).

^{1}H NMR (ppm, DMSO-d_6, 400 MHz, δ): **8.00 (t, 1H, 4.8Hz), 7.32~7.18 (m, 5H), 5.61 (m, 1H), 5.31 (m, 1H), 3.32 (m, 2H), 2.76 (t, 2H, 7.6Hz), 1.84 (s, 3H); ^{13}C NMR** (ppm, DMSO-d_6, 100 MHz, δ): **167.85, 140.52, 140.01, 129.09, 128.78, 126.52, 119.26, 41.00, 35.54, 19.11; Mass: exact mass 189.12, found 190.0. (Fig. S1, S2 (b))**

Synthesis of DPA46-2 (poly(DMA-co-PEG acrylate-co-PEGdiacrylate)) via RAFT polymerization

Copolymerization of DMA, PEG-acrylate (Mw = 480), and PEG-diacrylate (Mw = 550) was performed in DMF. DMA (88.4 mg, 0.4 mmol) was dissolved in 400 μl of DMF and added into a polymerization ampoule. PEG-acrylate (288.0 mg, 0.6 mmol) and PEG- diacrylate (11.5 mg, 0.02 mmol) were added to the ampoule. 0.5% mmol AIBN and RAFT agent (dibenzyl trithiocaronate) were dissolved in DMF (0.1 mg/μl) then added into the polymerization ampoule. After removing oxygen by three freeze-thaw cycles, polymerization was carried out at 70°C for 24 h. After completion, DPA462 was precipitated from diethyl ether: hexane (2: 1 volume ratio) twice, ~320 mg of a colorless high viscous polymer was obtained. Other polymers were polymerized under similar conditions via controlling the type and ratio of monomers (Table S1).

Polymerization

To synthesize the polymeric binders used in this study (DPA462, DPA552, DPA642), 40–60 mol% of DMA, 60–40 mol% of PEG-acrylate, and a small amount (2 mol%) of crosslinker (PEGDA) were incorporated (Table S1). Owing to the strong underwater adhesion of catechol moieties in DMA, inhibition of electrocatalyst detachment was expected in the synthesized polymeric binder. For control

experiments, PPA462 and BPA462 polymers constituting phenol and benzene, respectively, instead of catechol, were synthesized via the DPA462 polymerization method (Fig. S1 and Table S1).

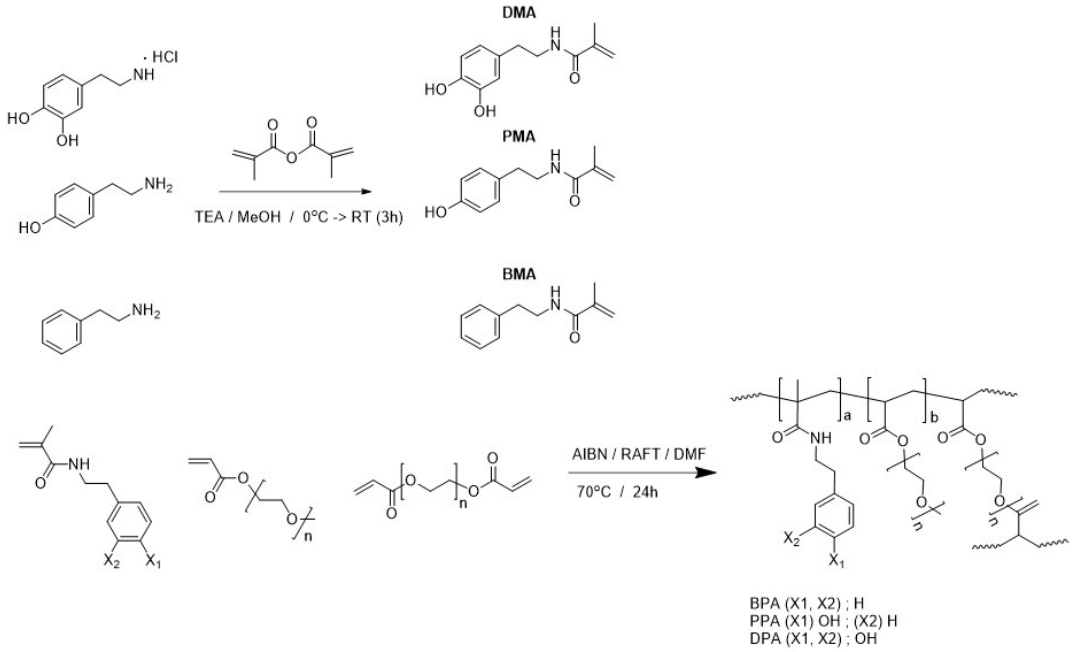

Scheme S1. Synthetic route of PMA, BMA monomers, and polymers.

Table S1. Formulation of hydrophilic polymers.

	BMA	PMA	DMA	PEG-acrylate	PEG-diacrylate	AIBN	RAFT
				(mg)			
DPA462	-	-	88.4	288.0	11.5	0.82	1.45
DPA552	-	-	110.5	240.0			
DPA642	-	-	132.6	192.0			
BPA462	75.7	-	-	288.0			
PPA462	-	82.1	-	288.0			

(a)

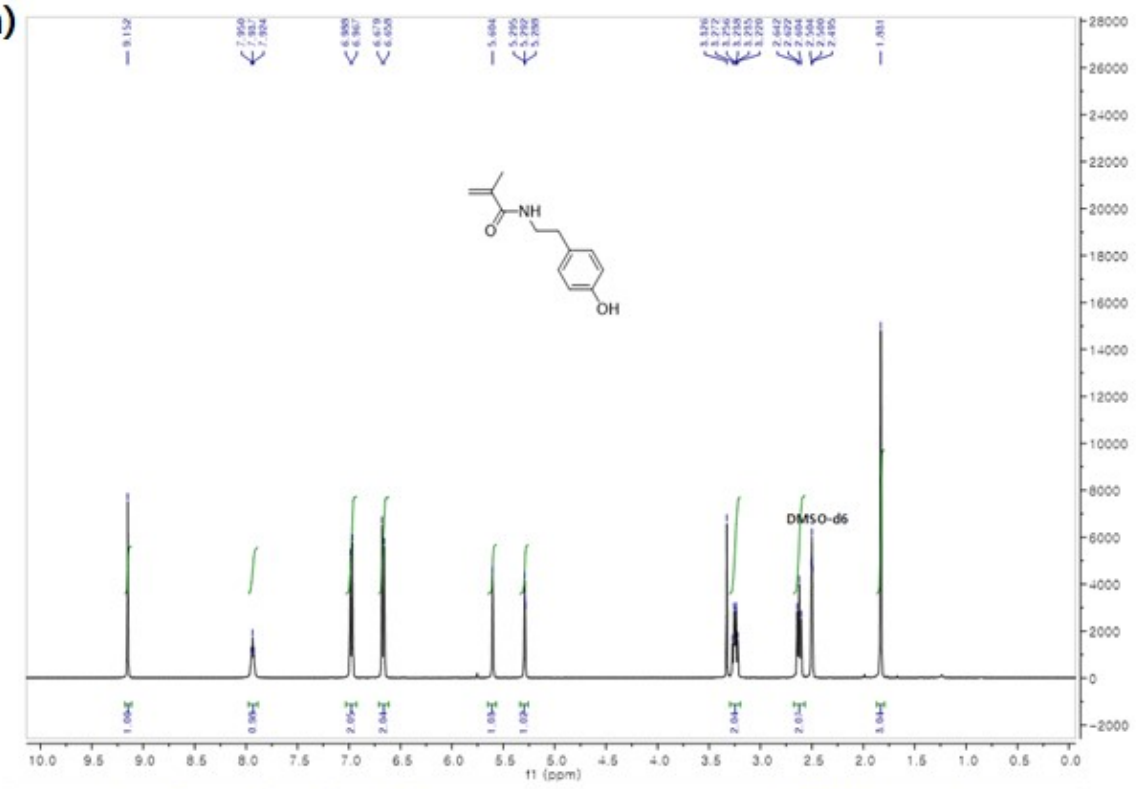

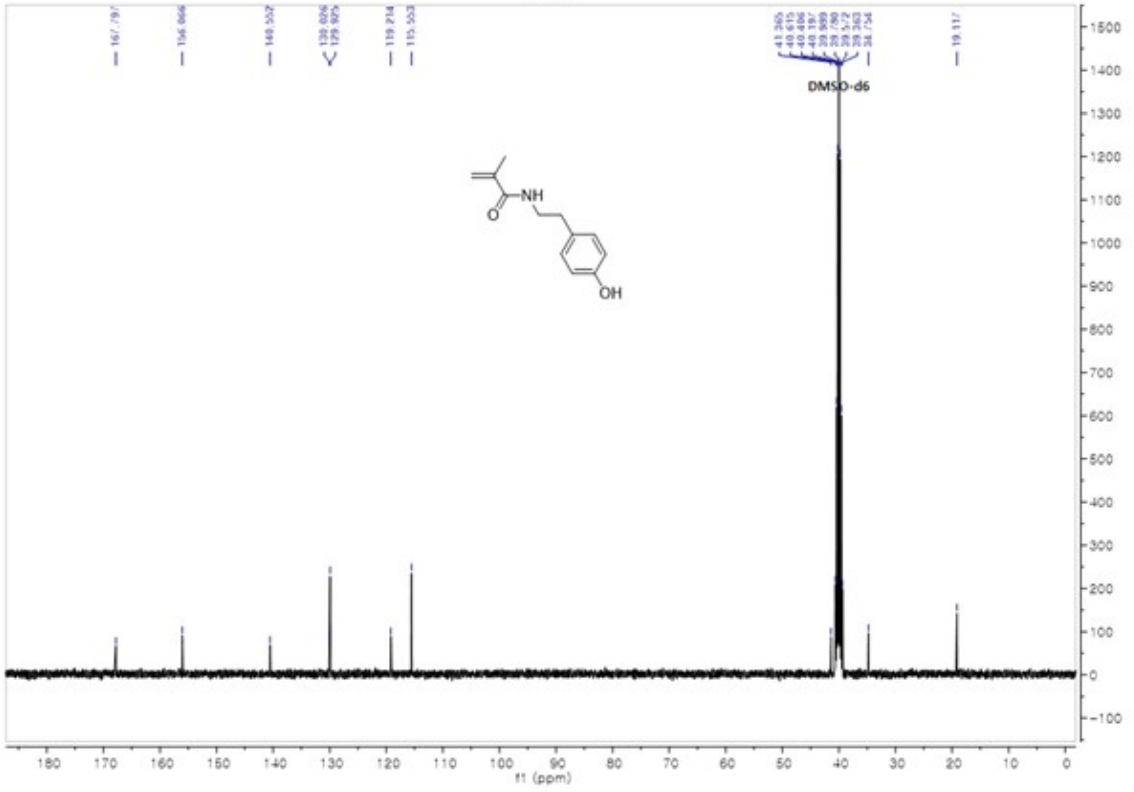

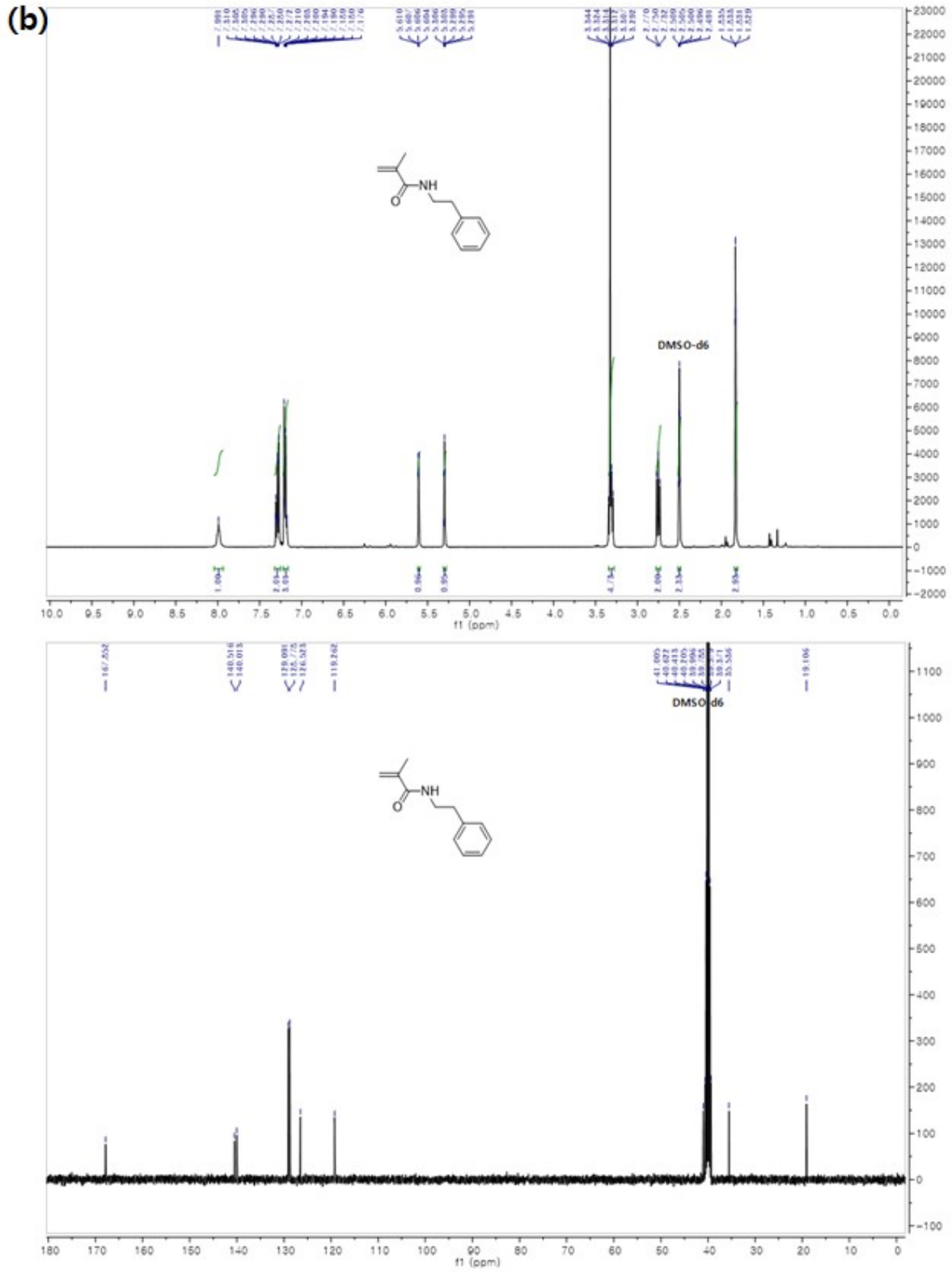

Fig. S1 ^{1}H, ^{13}C-NMR of (a) PMA and (b) BMA.

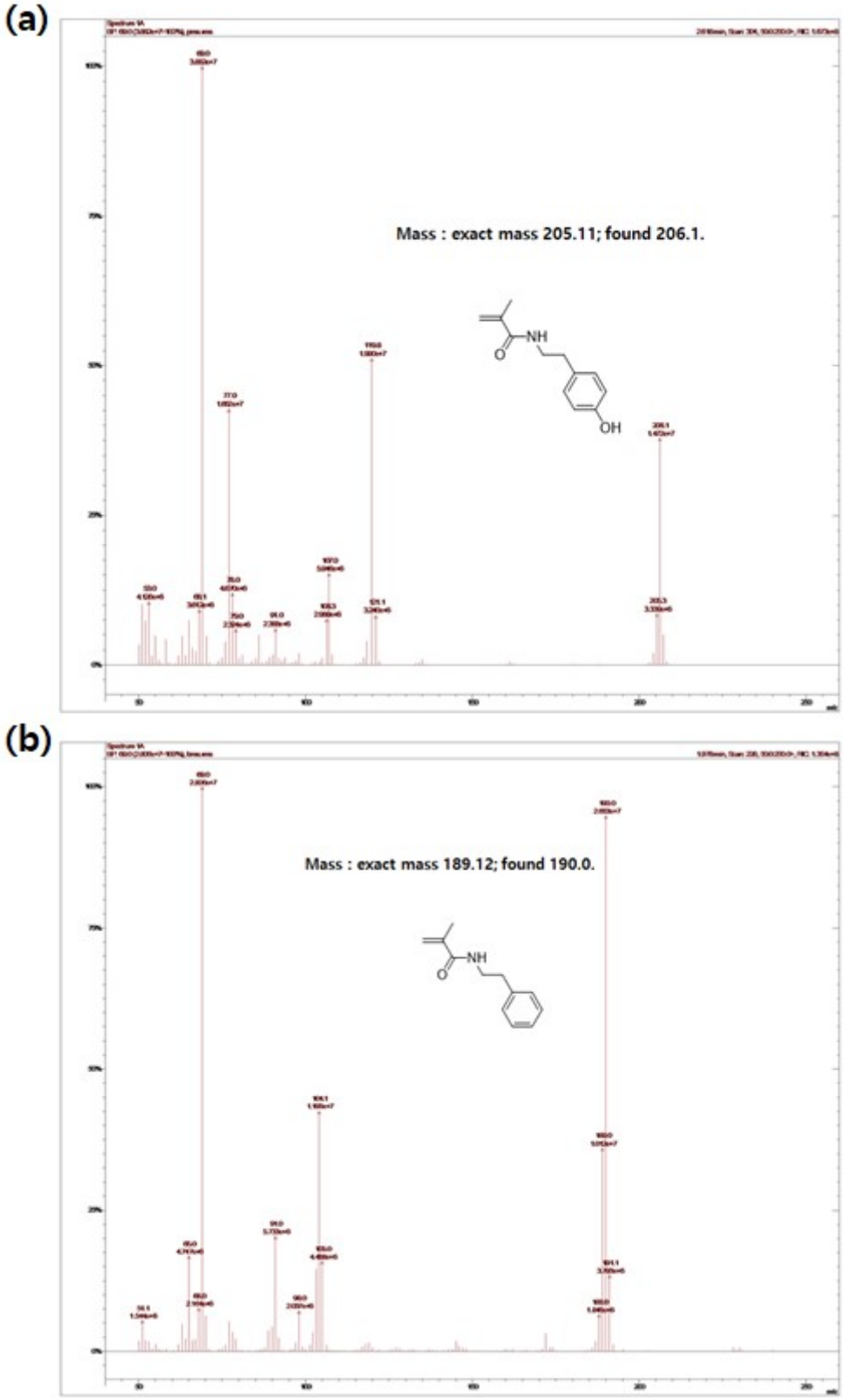

Fig. S2 ICP-Mass spectrum of (a) PMA and (b) BMA.

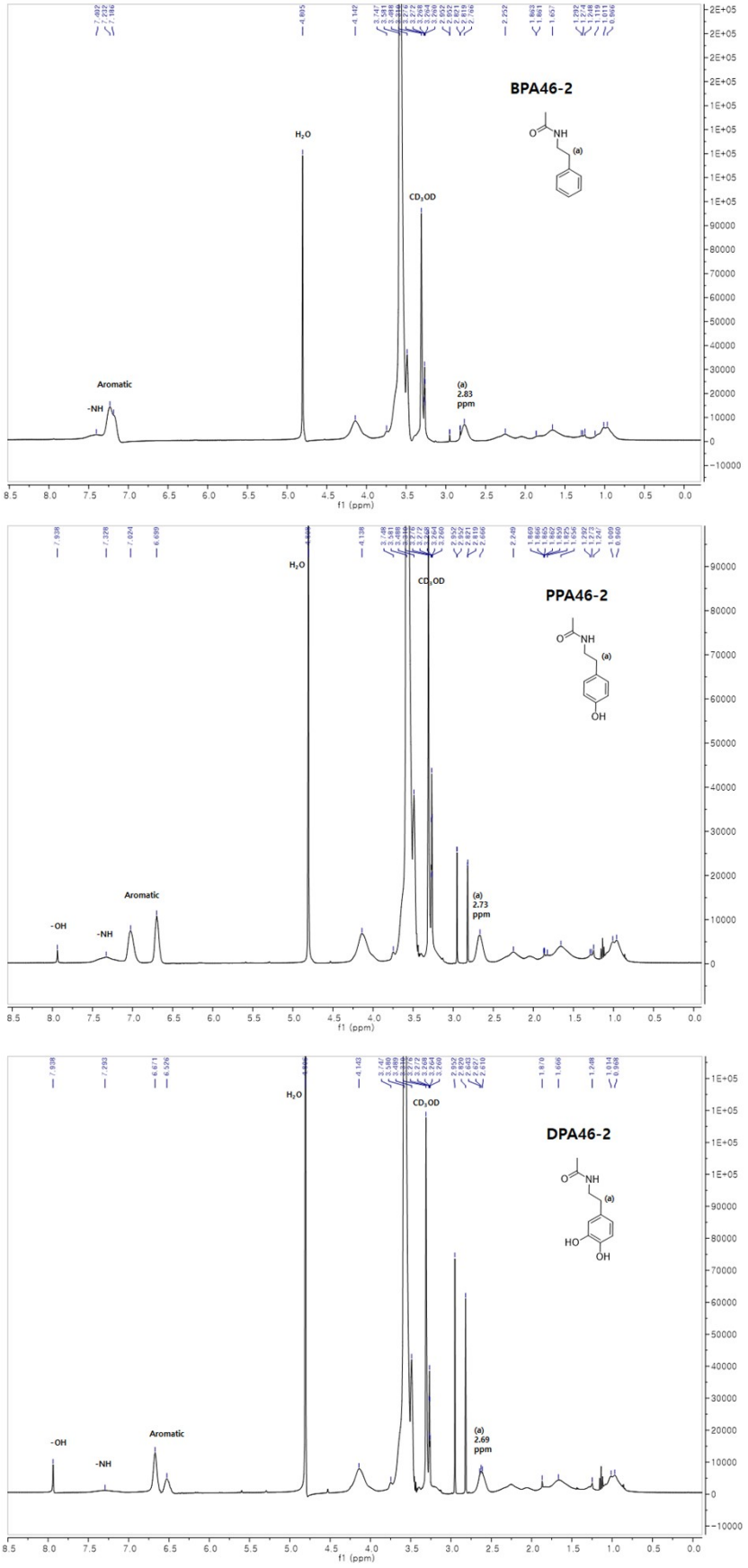

Fig. S3 [1]H-NMR spectra of BPA462, PPA462 and DPA462 polymers.

Thermal properties of polymers

Fig. S4 and table S2 show the thermal properties (DSC and TGA) of polymers. The observed glass transition temperatures (Tg) are in the following order: DPA642 > DPA552 > DPA462 > PPA462 > BPA462. More number of OH groups and higher catechol contents induces enhanced intermolecular hydrogen bonding, causing higher Tg. TGA of the polymers showed 5 wt% degradation temperature at 290°C, indicating that they are sufficiently thermally stable for applications in SABs.

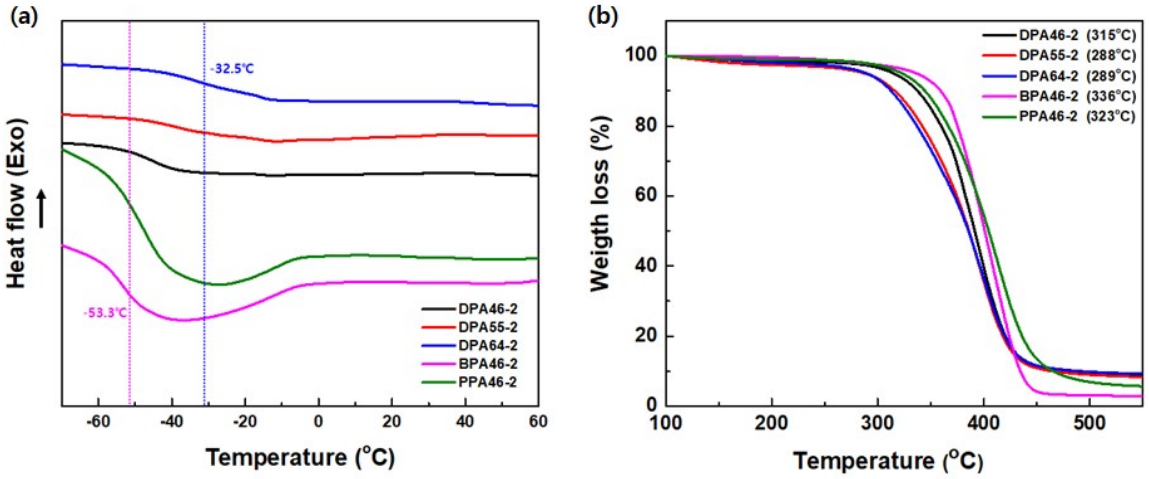

Fig. S4 Thermal properties of polymers ; (a) DSC and (b) TGA.

Table S2. Thermal transition and 5 wt% degradation temperature of polymers.

	Tg (℃)	T_{5d} (℃)
DPA462	-44.9	315
DPA552	-38.6	288
DPA642	-32.5	289
BPA462	-53.3	336
PPA462	-48.3	323

Rheology properties of polymers

Rheological analysis of the DPA series based on catechol content showed that the loss modulus (G") was greater than the storage modulus (G'). In addition, higher catechol content polymers showed larger G" and G' values. The increase in modulus values can be explained by the increase in hydrogen bonding that occurs at higher catechol content. (Fig. S5a). An increase in the number of OH groups also causes higher modulus values owing to hydrogen bonding (Fig. S5b).

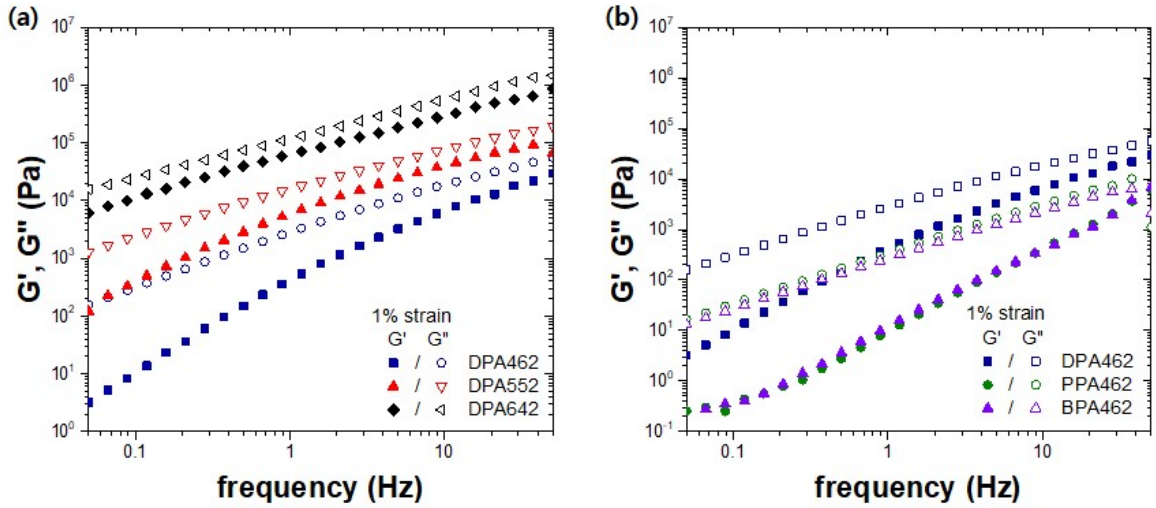

Fig. S5 Frequency sweep of polymer series with storage (G') and loss (G'') moduli reported as closed and open symbols; (a) DPA polymers, (b) BPA, PPA and DPA462 polymers.

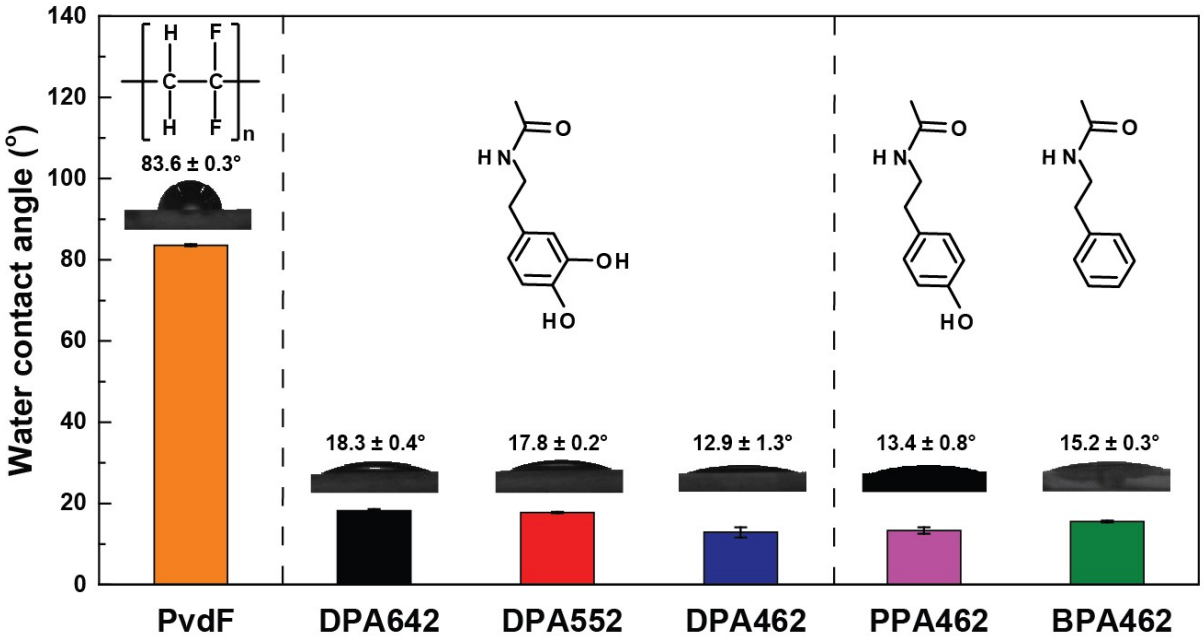

Fig. S6 Bar graph and droplet image showing the water contact angle of polymer-coated glass surfaces.

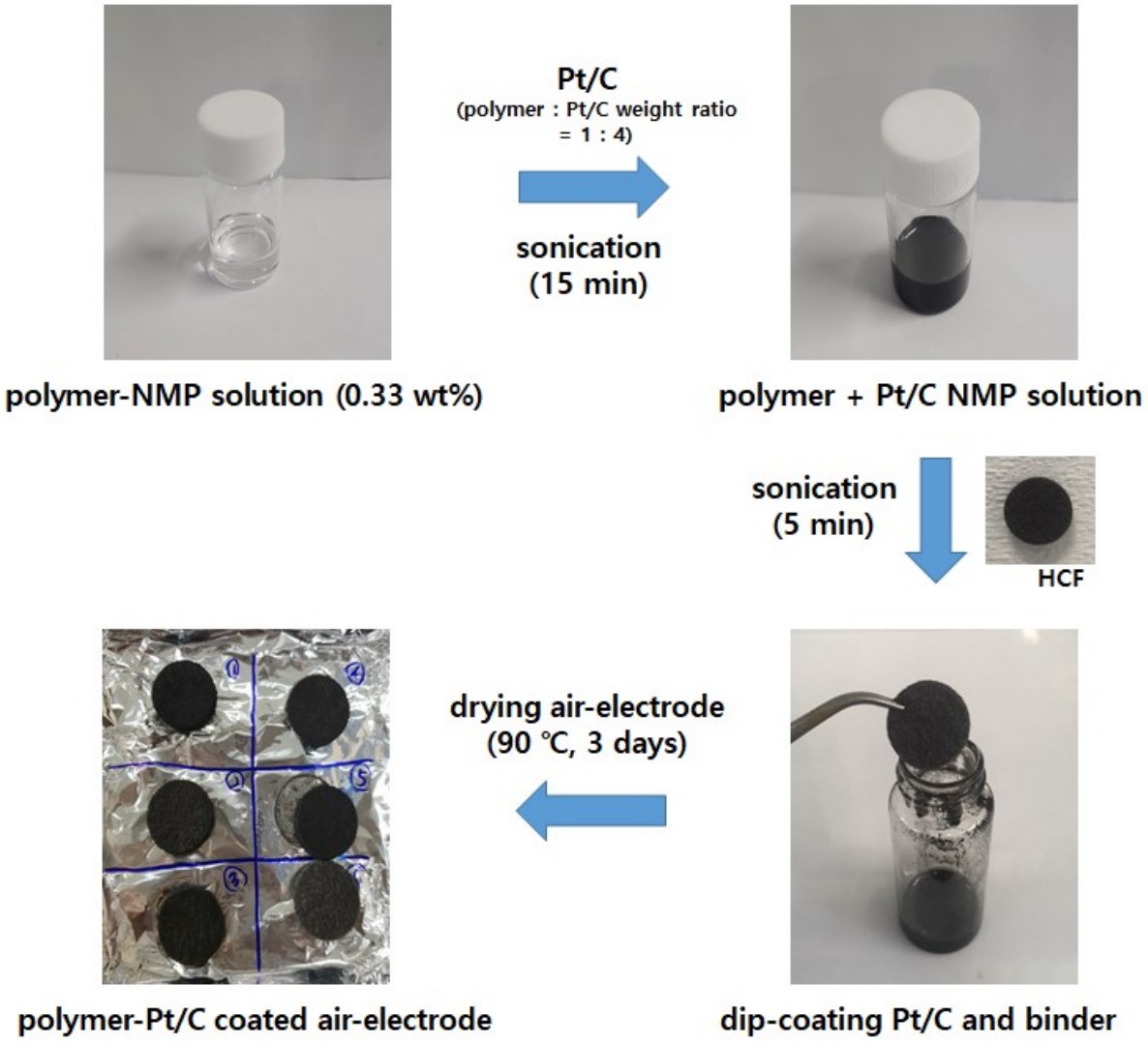

Scheme S2. Preparation of air-electrode for SABs.

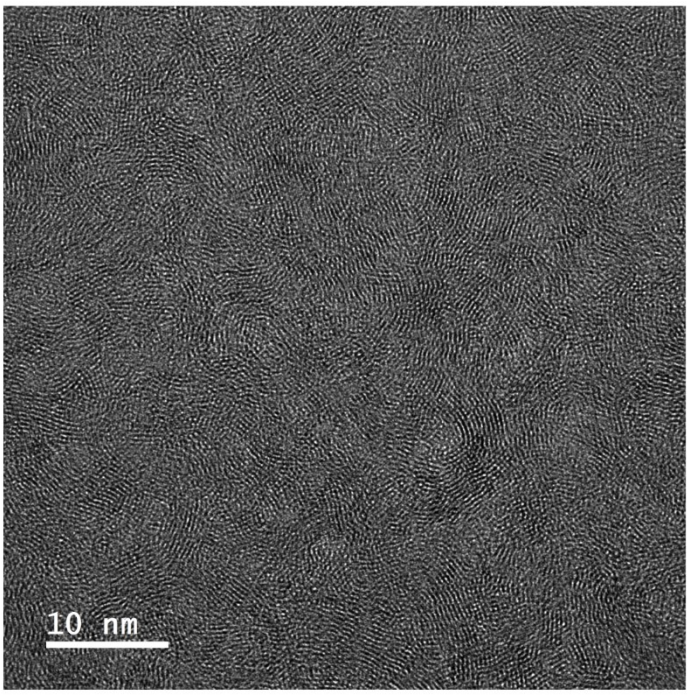

Fig. S7 HR-TEM image of the bulk side of a graphitic carbon felt.

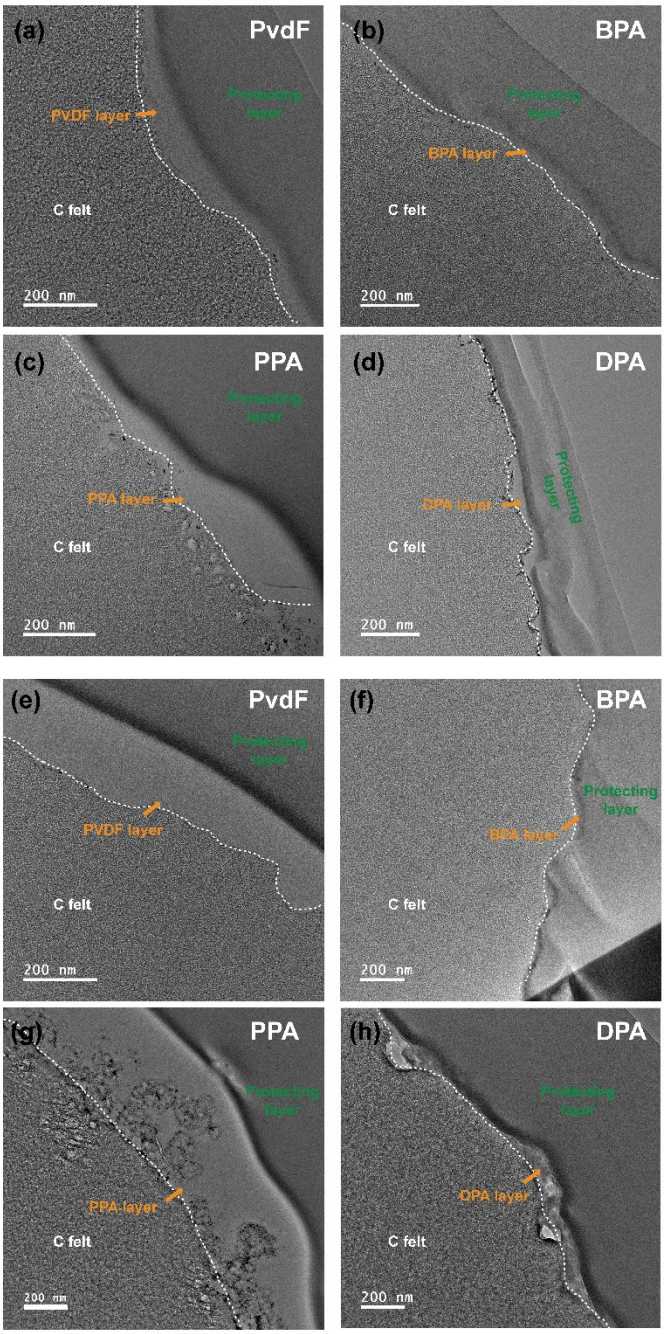

Fig. S8 Low magnification TEM images of Pt/carbon composites with polymer binders before battery cycle (a) PvdF, (b) BPA, (c) PPA, and (d) DPA and after battery cycle (e) PvdF, (f) BPA, (g) PPA, and (h) DPA.

Metal-coordination of polymer binder

The Fourier-transform infrared spectroscopy (FT-IR) spectra were recorded using a JASCO FT/IR 4600 spectrometer. To identify the metal-coordination bonding between Pt catalyst and DPA binder, FT-IR spectrum of the electrocatalyst (Pt/C)-DPA642 binder mixture (Fig. S9) was compared with that of pure DPA642 binder. The FT-IR spectra of both samples showed peaks related to hydroxyl groups: the peak around 3350 cm-1 corresponds to –OH stretching, and the peaks 1255 cm-1 and 1285 cm-1 corresponds to C-OH stretching. The FT-IR spectrum of Pt/C-DPA642 mixture showed intensity reduction of –OH and C-OH peaks due to metal-coordination between DPA642 and Pt/C.

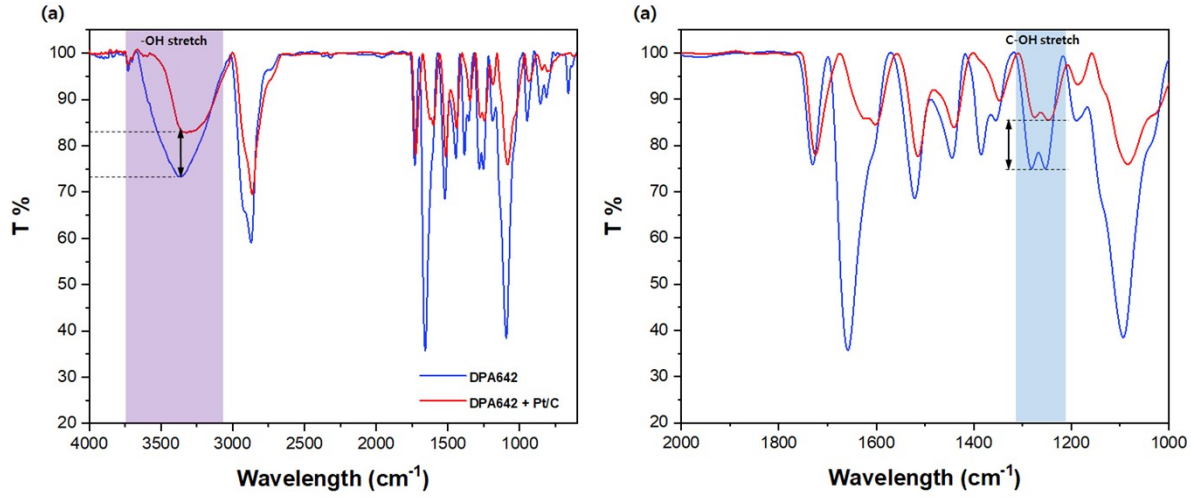

Fig. S9 FT-IR spectra of pure DPA642 binder (blue line) and Pt/C catalyst-DPA642 mixture (red line) of (a) -OH stretching and (b) C-OH stretching of catechol.

Self-healing experiments

A 2.2 g synthesized DPA642 polymer was placed between Teflon films, and an external force was applied by a 2.5 kg roller to make the polymer a smooth planar shape with constant thickness. The DPA642 polymer with Teflon films was dried for 2 days in an oven (high vacuum condition, 40°C) to eliminate air bubbles. Afterward, DPA642 was placed on a microscope slide (2.5 × 2.5 cm^2) and scratched using a ceramic blade. The slide glass was cut by a glass cutter, rinsed twice with ethanol and acetone to remove the microscope slide polishing surface, and dried using N_2 blowing gun. All self-healing processes were spontaneously performed at room temperature in the air. An optical microscope (FLIR, Grasshopper3) was used for observing the self-healing behavior of films. Time-lapse images were taken every 1 min until the film healed.

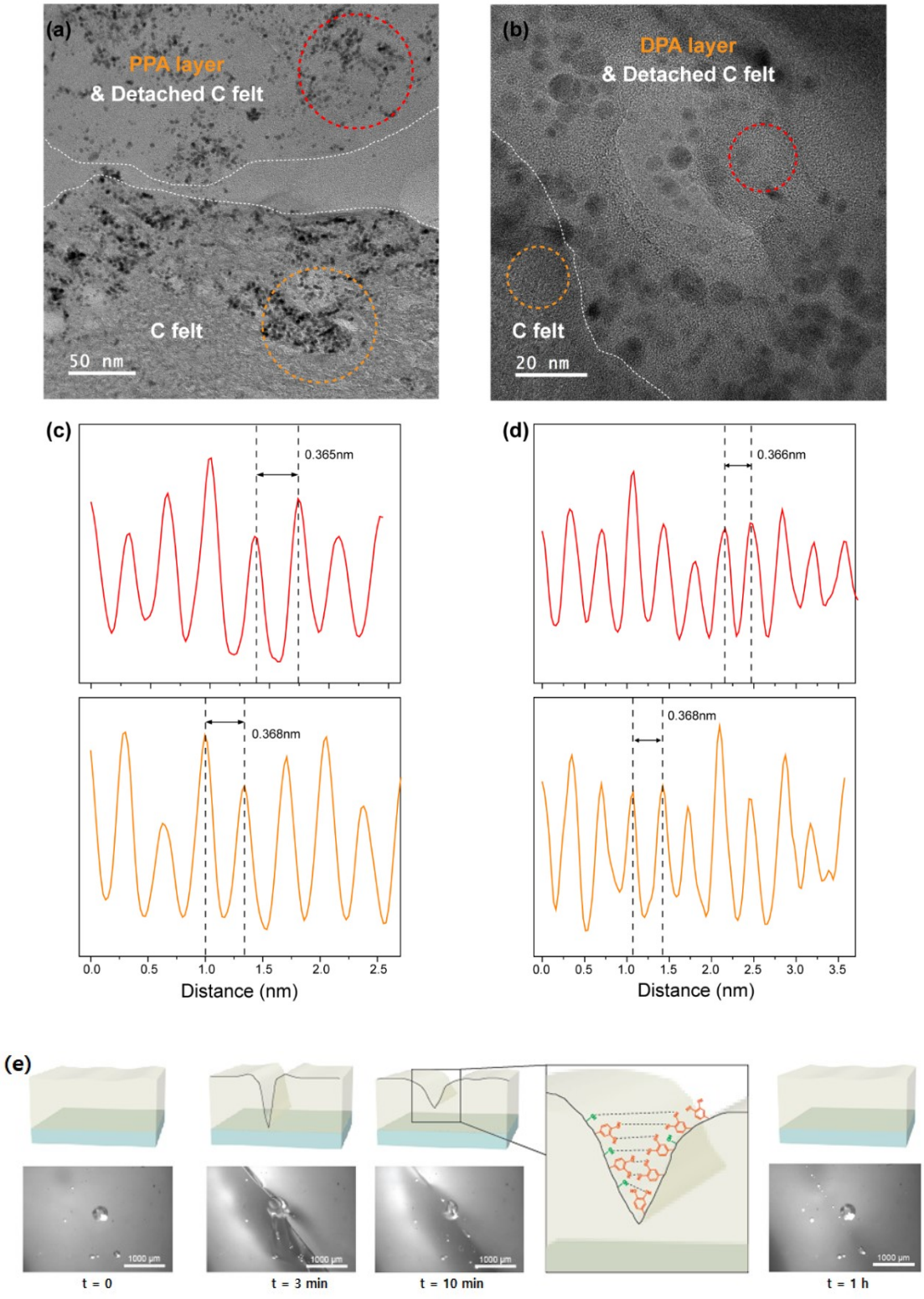

Fig. S10 Lattice fringe comparison of the graphitic carbon layers between carbon felt and the detached Pt/carbon felt cluster in (a, c) PPA and (b, d) DPA composites. The lattice fringes of the graphitic carbon regions on the polymer layers (red circle in a and b) were well matched with the lattice fringes of the original carbon felt (orange circle in a and b). (e) DPA self-healing performance under room temperature.

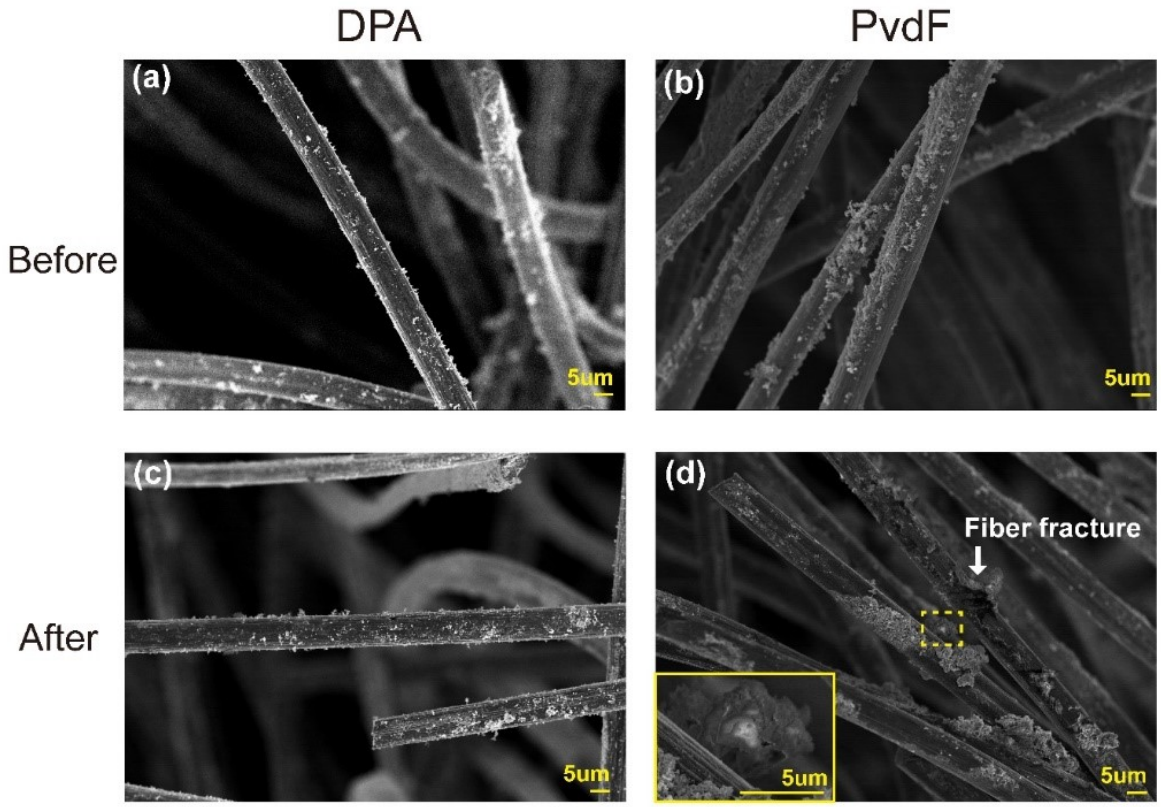

Fig. S11. Scanning Electron Microscope (SEM) images of DPA and PvdF coated electrodes before and after 100 charge-discharge cycles. Before cycling, (a) DPA and Pt/C were evenly coated to the HCF surface, while (b) for PvdF coated HCF, aggregates were observed resulting in an uneven and rough coating on the HCF. After 100 charge-discharge cycles, (c)noticeable structural changes were not observed for DPA coated HCF, while (d) PvdF coated HCF showed fracturing of carbon fibers and petal-like intermediate structure which are known to be evidence of carbon corrosion upon oxidation[3]. The inset of (d) shows the zooming in the yellow dotted square showing petal-like intermediate structure.

Surface preparation for Surface Force Apparatus (SFA).

To prepare polymer-coated surfaces, 0.3 μl of DPA series, PPA462, BPA462 and PvdF polymer solutions (5 wt.%, Ethanol) were dropped on to the spherical glass discs (Radius, R ~ 1 cm), followed by drying at room temperature for 10 min. As adherend surfaces, Pt surface and heat-treated carbon felt (HCF) are prepared. For Pt Surface, the (111) plane of Pt layer (~30 nm) was deposited on the Si wafer using an E-beam evaporator (FC-2000, Ferro Tec, Temescal, USA). The carbon felt [carbon nanofibers (CNFs), soft felt (PAN-based) 3 mm thickness] was heat-treated at 500°C for 4 h in a muffle furnace (LEF-105S-1, Daihan Labtech Co Ltd; Namyangju, Korea). Then, the prepared adherend surfaces were glued on a flat glass disk using a UV glue (NOA 81, Norland Products, NJ, USA).

Surface Force Apparatus experiments

Fig. S12 shows a schematic of the SFA experimental set-up for adhesion force measurement (Fig. S12a) and representative adhesion profile at a constant load (Fig. S12b). The adhesive force profile was calculated as a function of the voltage by a series of signals from z-axis of the 3D actuators, which is directly connected to a signal conditioning amplifier (2310B, Vishay, Malvern, USA). A data acquisition system (RA2300, A&D, Tokyo, Japan) was used to record adhesion and load profiles from the signal conditioning amplifier. The strain gauge connected to 3D sensor/1D actuator was calibrated at the beginning of the experiment by converting corresponding load to voltage. Two surfaces were pressed until reach at a desired load (200 mN) and followed by separation. Every force measurement was repeated at least 5 times with 5 different contact points to confirm reproducibility.

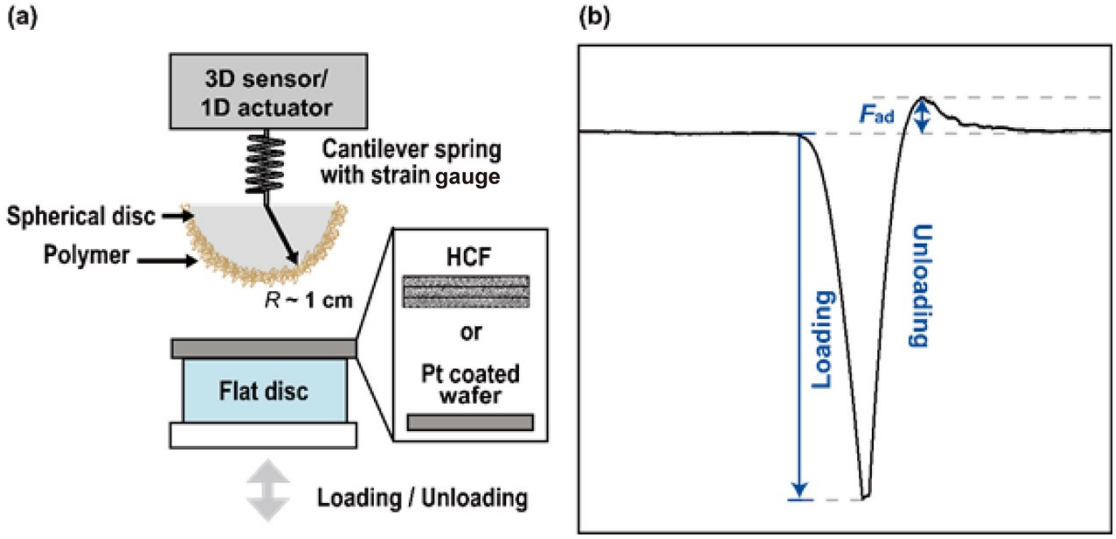

Fig. S12 (a) A schematic of the SFA experimental set-up for adhesion force measurement and (b) representative loading, unloading, and adhesion signal during the measurement.

Calculation details

Fig. S13 shows the model systems of our interest. We considered the Pt (111) surface and pristine/functionalized graphene, which represented HCF, to investigate the binding energies of DPA, PPA, and BPA as the binding units of the polymers on Pt and HCF substrates (Fig. S13a). For the Pt surface, we used the (111) crystal plane, because it was reported to be the most thermodynamically stable[4] and abundant plane of Pt (Fig. S13b).[5,6] The size was 13.87 Å × 13.87 Å adopting experimental lattice constant (*i.e.*, 3.9239 Å).[7] The Pt model system comprises three atomic layers consisting of 25 atoms in each layer. The vacuum region of 20 Å perpendicular to the surface was applied to avoid self-interaction. The two bottom layers were fixed to theoretically describe the bulk phase. Based on the experimental X-ray photoelectron spectroscopy (XPS) analysis of HCF (Fig. S15), the oxygen-containing functional groups were considered (*i.e.*, hydroxyl, epoxy, carbonyl, and carboxyl). We adopted the Lerf–Klinowski model[8], which is the most frequently represented for functionalized graphene to represent HCF. The basal plane of pristine graphene, the 14.76 Å × 14.76 Å size, was optimized, including a 20 Å of vacuum slab along the *z*-direction. In detail, the hydroxyl and epoxy groups were introduced on the graphene basal plane (Fig. S13c), whereas hydroxyl, carbonyl, and carboxyl groups were attached to the ZZ and AC edges (Fig. S13d).

The binding energy ($\Delta E_{binding}$) of DPA-, PPA-, and BPA-adsorbed on the Pt (111) surface or HCF was calculated as follows:

$$\Delta E_{binding} = E_{substrate+X} - E_{substrate} - E_X$$

[*substrate* = Pt (111) surface and HCF; *X* = DPA, PPA, and BPA]

where $E_{surbstrate+X}$ is the total energy of *X* adsorbed on a substrate, and $E_{substrate}$ and E_X are the total energies of the adsorbed substrate (*i.e.*, Pt (111) surface or HCF) and the total energies of adsorbates *X* (*i.e.*, DPA, PPA, and BPA), respectively. For HCF, the binding energy was calculated by considering the weight factor obtained from experimental XPS analysis for each function group binding energy contribution (Table S3). The $\Delta E_{binding}$ of each functional group is the average of the model system

considered as follows:

$$\Delta E_{binding,\,HCF}^{\;X} = \frac{74.39}{100} \times \Delta E_{binding,\,aromatic}^{\;X} + \frac{10.75}{100} \times \Delta E_{binding,\,hydroxyl}^{\;X} + \frac{3.69}{100} \times \Delta E_{binding,\,epoxy}^{\;X} + \frac{6.38}{100} \times \Delta E_{binding,\,carbonyl}^{\;X} + \frac{4.90}{100} \times \Delta E_{binding,\,carboxyl}^{\;X}$$

(X = DPA, PPA, and BPA)

To understand the interaction between the adsorbates (*i.e.*, DPA, PPA, and BPA) and Pt (111) surface, electron density difference was calculated as follows:

$$\Delta\rho = \rho(Pt + X) - \rho(Pt) - \rho(X), \text{ [}X\text{ = DPA, PPA, and BPA]}$$

where $\rho(Pt + X)$ is the electron density of X adsorbed on Pt (111) surface; $\rho(Pt)$ is the electron density of Pt surface; $\rho(X)$ is the electron density of DPA, PPA, and BPA.

$\Delta E_{binding}$ of functional groups on HCF

The adsorption structures and $\Delta E_{binding}$ of DPA, PPA, and BPA on each functional group of HCF are shown in Fig. 3g–k, S14 and S16. The distances ($d_{z,\,avg}$) between the pristine graphene and DPA, PPA, and BPA are well-related to $\Delta E_{binding}$: DPA-adsorbed graphene case ($d_{z,\,avg}$ = 3.439 Å, $\Delta E_{binding}$ = −32.22 kcal/mol), which is more stable than PPA ($d_{z,\,avg}$ = 3.507 Å, $\Delta E_{binding}$ = −27.95 kcal/mol) and BPA ($d_{z,\,avg}$ = 3.533 Å, $\Delta E_{binding}$ = −26.04 kcal/mol), shows the closest approach to graphene. In adsorption with the hydroxyl group, DPA exhibited higher $\Delta E_{binding}$ than PPA and BPA, showing that the number of hydrogen bonds between the adsorbate and hydroxyl group on graphene correlates to $\Delta E_{binding}$. However, for epoxy, carbonyl, and carboxyl functional groups, DPA showed lower $\Delta E_{binding}$ than PPA, attributed to the intramolecular hydrogen bonding of DPA, which weakened the hydrogen bonding with the functional groups on graphene. However, since the proportion of epoxy (3.58%), carbonyl (6.38%), and carboxyl (4.90%) in HCF is much smaller than that of graphene (74.38%) and hydroxyl (10.75%) (Table S3), we can expect that DPA will bind stronger than PPA and

BPA.

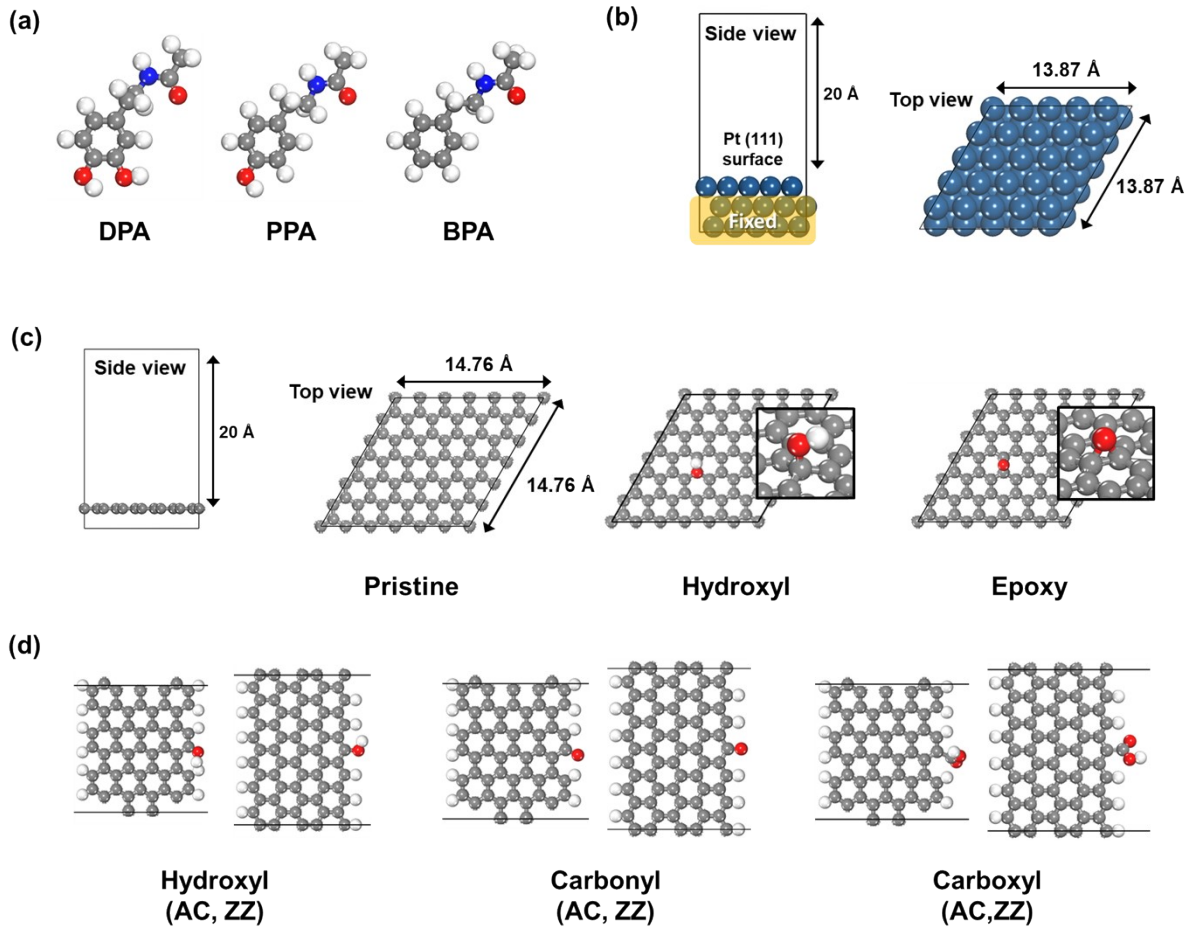

Fig. S13 Model systems of (a) binding unit of DPA, PPA, and BPA, (b) Pt (111) surface, (c) basal plane systems of pristine, hydroxide, and epoxide-functionalized graphene, and (d) edge systems of armchair (AC) and zigzag (ZZ) nanoribbons with hydroxyl, carbonyl, and carboxyl groups. Platinum, carbon, oxygen, nitrogen, and hydrogen are colored with navy, gray, red, blue, and white, respectively.

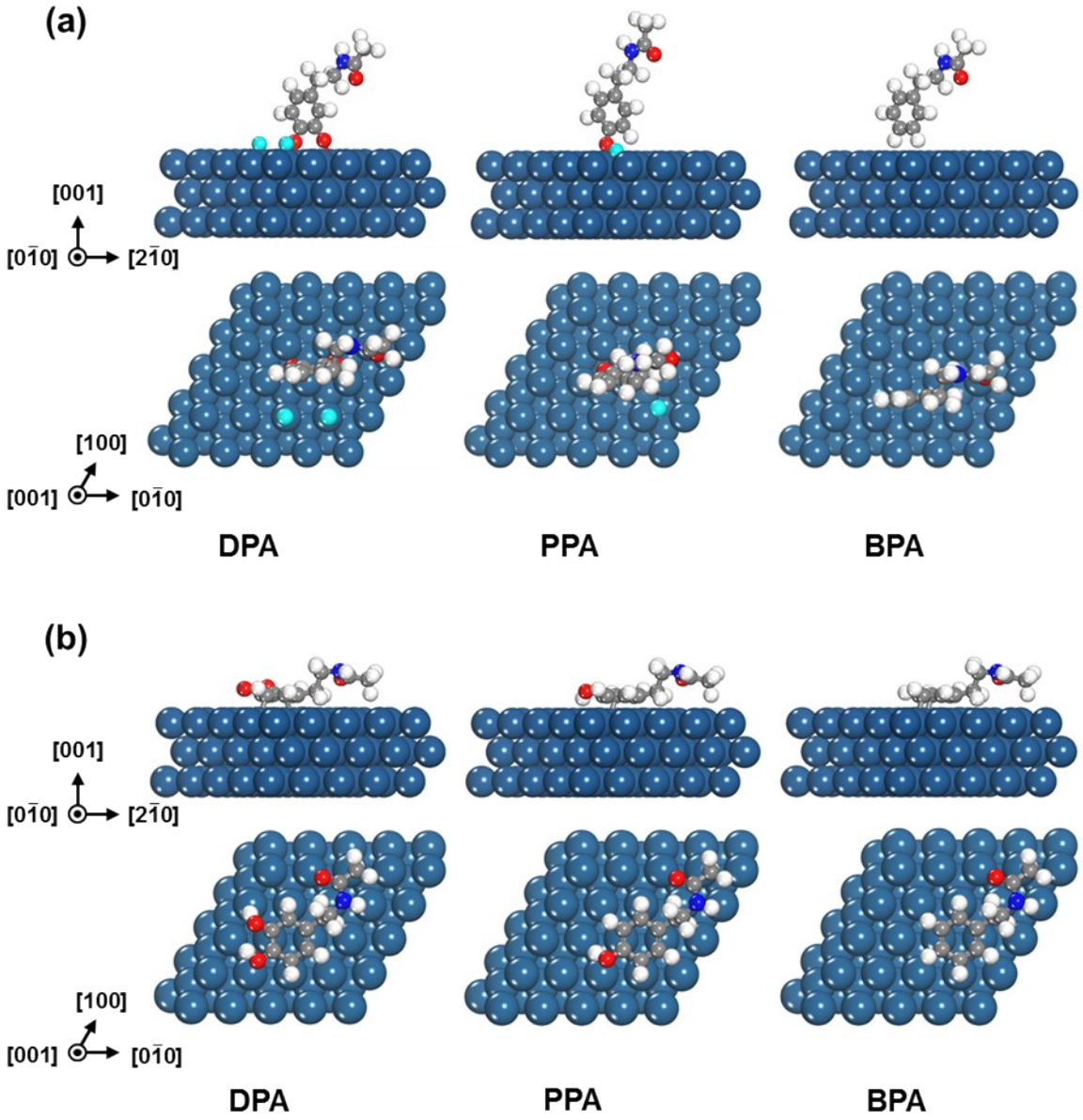

Fig. S14 Optimized adsorbed structures of DPA, PPA, and BPA on the Pt (111) surface for (a) dissociative adsorption and (b) molecular adsorption. Platinum, carbon, oxygen, nitrogen, hydrogen, and deprotonated hydrogen atoms are colored with navy, gray, red, blue, white, and cyan, respectively.

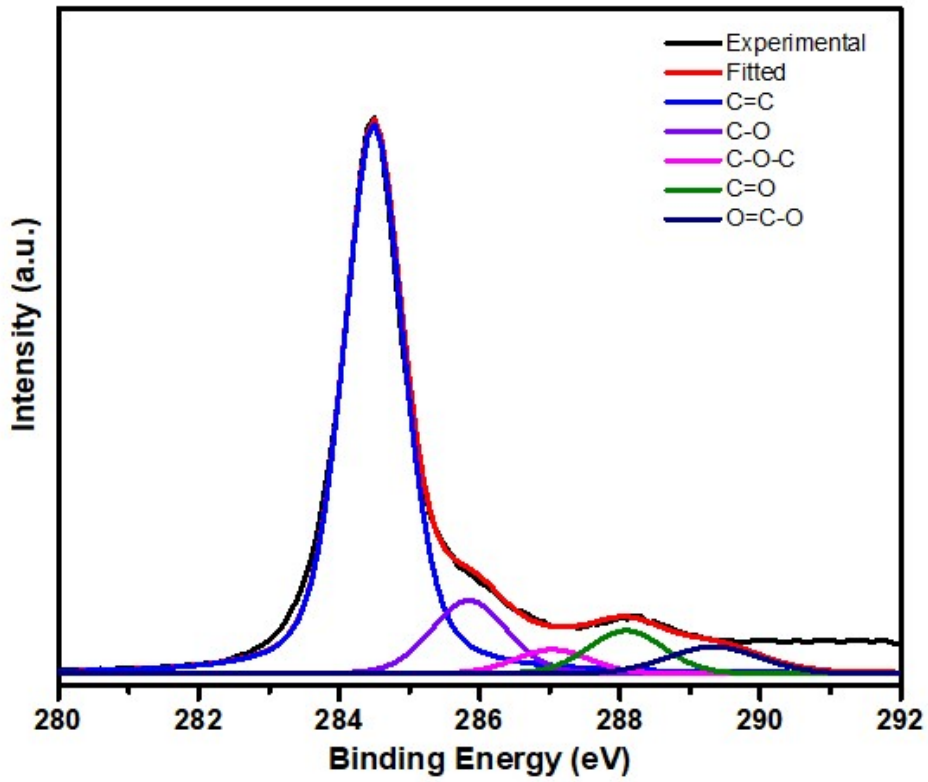

	C=C	C-O	C-O-C	C=O	O=C-O
Carbon felt (%)	74.39	10.75	3.69	6.38	4.90

Fig. S15 C1s XPS spectra of HCF (percentage of functional group binding energy).

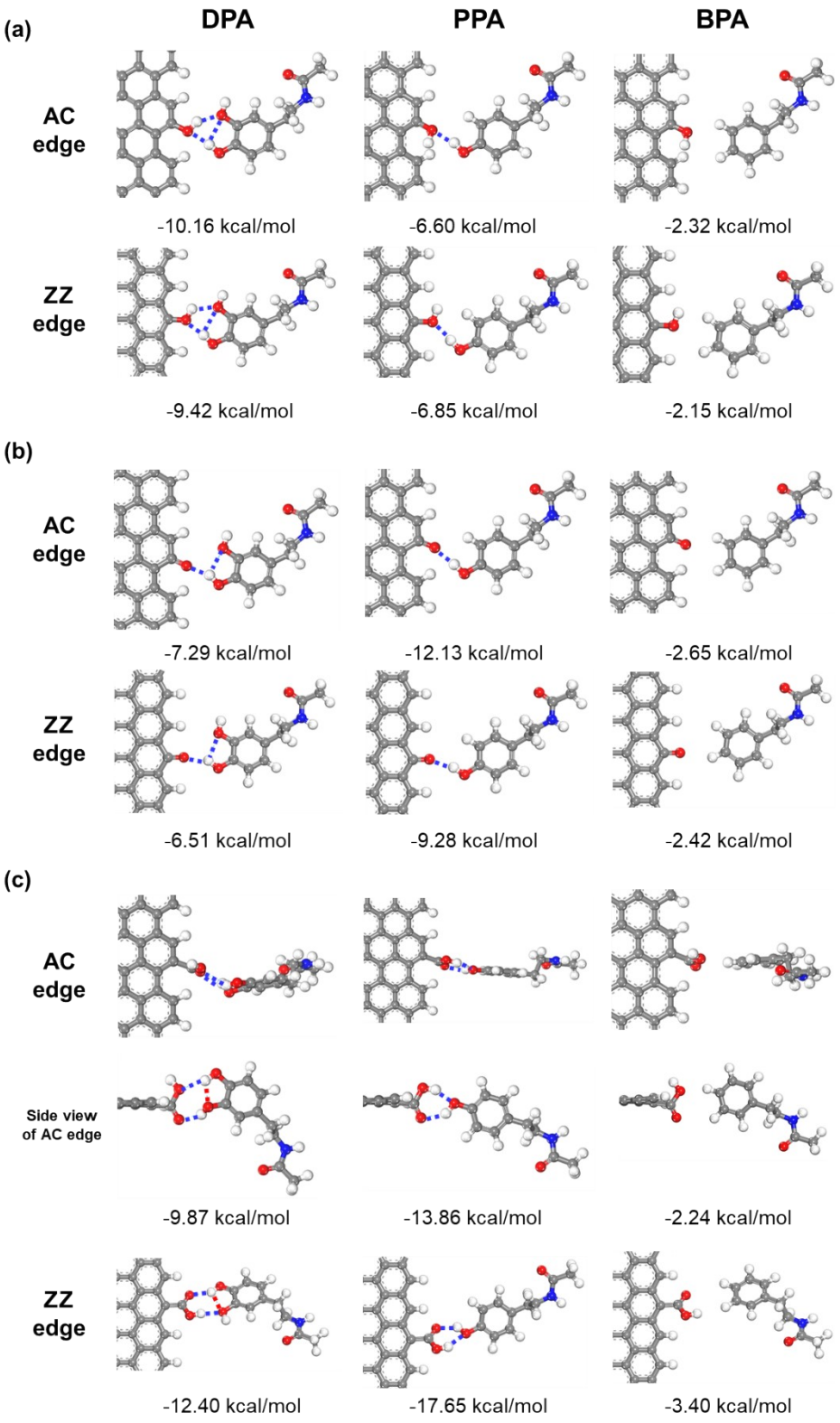

Fig. S16 Optimized adsorption structures with $^{\Delta E_{binding}}$'s of DPA, PPA, and BPA on edges (*i.e.*, AC and ZZ) of nanoribbon models with (a) hydroxyl group, (b) carbonyl group, and (c) carboxyl group.

Table S3. Binding energies of functional groups in HCF.

			$\Delta E_{binding}$ **(kcal/mol)**	**Proportion (%)**	**relative** $\Delta E_{binding}$ **(kcal/mol)**	**Total** $\Delta E_{binding}$ **(kcal/mol)**
DPA	Aromatic	Basal plane	-32.22	74	-23.96	-28.06
	Hydroxyl	Basal plane	-40.19	4	-1.44	
		AC edge	-10.16	4	-0.36	
		ZZ edge	-9.42	4	-0.34	
	Epoxy	Basal plane	-30.48	4	-1.09	
	Carbonyl	AC edge	-7.29	3	-0.23	
		ZZ edge	-6.51	3	-0.21	
	Carboxyl	AC edge	-9.87	2	-0.24	
		ZZ edge	-12.40	2	-0.30	
PPA	Aromatic	Basal plane	-27.95	74	-20.79	-24.95
	Hydroxyl	Basal plane	-37.26	4	-1.34	
		AC edge	-6.60	4	-0.24	
		ZZ edge	-6.85	4	-0.25	
	Epoxy	Basal plane	-33.12	4	-1.19	
	Carbonyl	AC edge	-12.13	3	-0.39	
		ZZ edge	-9.28	3	-0.30	
	Carboxyl	AC edge	-13.86	2	-0.34	
		ZZ edge	-17.65	2	-0.43	
BPA	Aromatic	Basal plane	-26.04	74	-19.37	-21.87
	Hydroxyl	Basal plane	-28.57	4	-1.02	
		AC edge	-2.32	4	-0.08	
		ZZ edge	-2.15	4	-0.08	
	Epoxy	Basal plane	-28.19	4	-1.01	
	Carbonyl	AC edge	-2.65	3	-0.08	
		ZZ edge	-2.42	3	-0.08	
	Carboxyl	AC edge	-2.24	2	-0.05	
		ZZ edge	-3.40	2	-0.08	

Electrochemical properties

The electrochemical performance of SABs is shown in Fig. S17-22. As the number of OH groups decreases (from DPA462 to BPA462), the gap of charge/discharge voltage expanded significantly (DPA ~1.1 V and BPA ~1.6 V at 50 cycles). BPA462 exhibits poor adhesion against Pt/C and HCF, so it is believed that a large number of Pt catalyst desorption rapidly occurred during the first few charge/discharge cycles. Further, the charging/discharging performance DPA series shows a similar voltage difference; however, the maximum power of DPAs has a distinction from 14.7 (DPA462) to 12.0 mW (DPA642) (Fig. S21), which is owing to the wettability caused by the ratio of catechol and PEG groups.

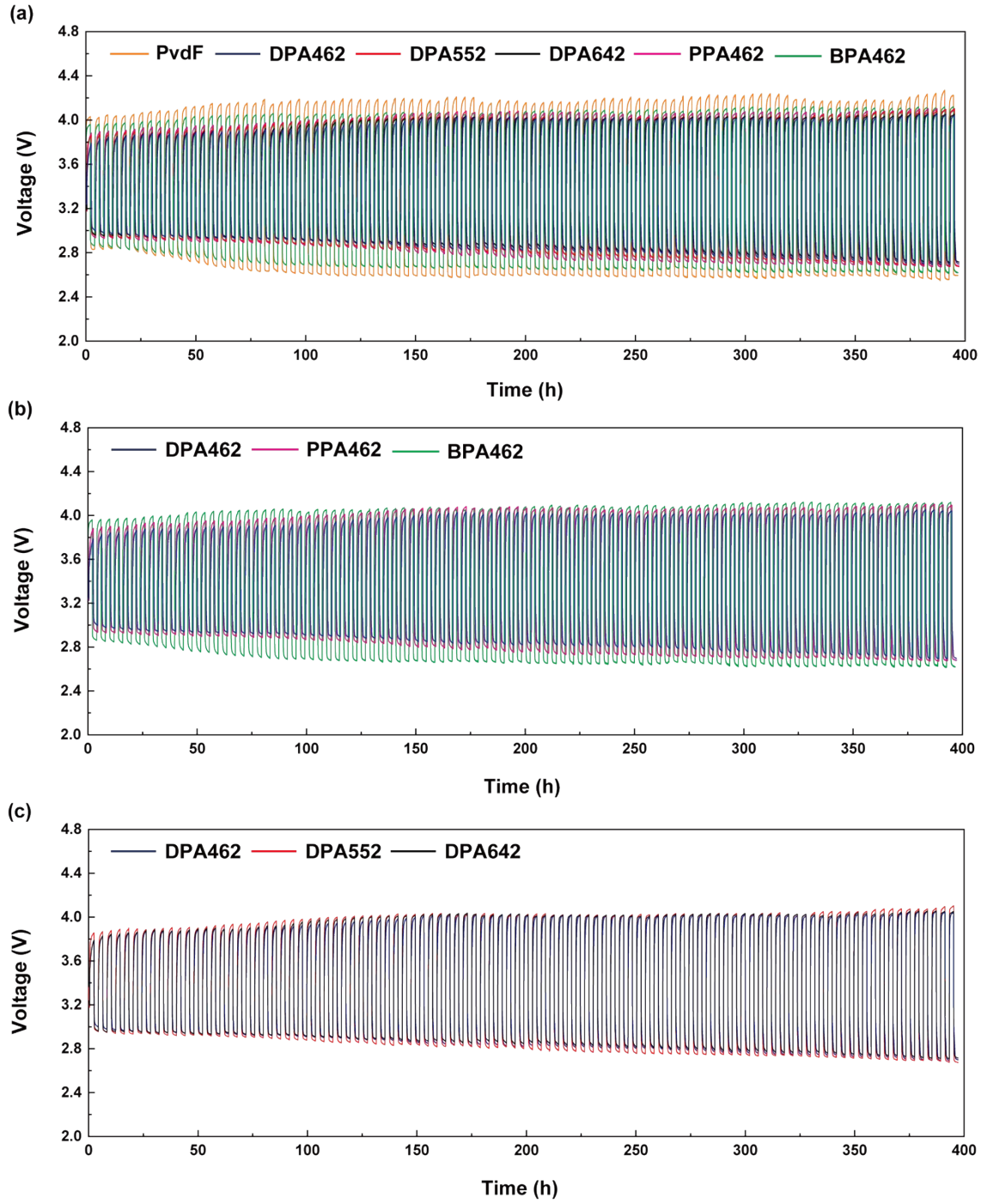

Fig. S17 Galvanostatic charge/discharge performances of (a) synthesized and PvdF binders, (b) DPA462, DPA552 and DPA642, and (c) DPA462, PPA462, and BPA462.

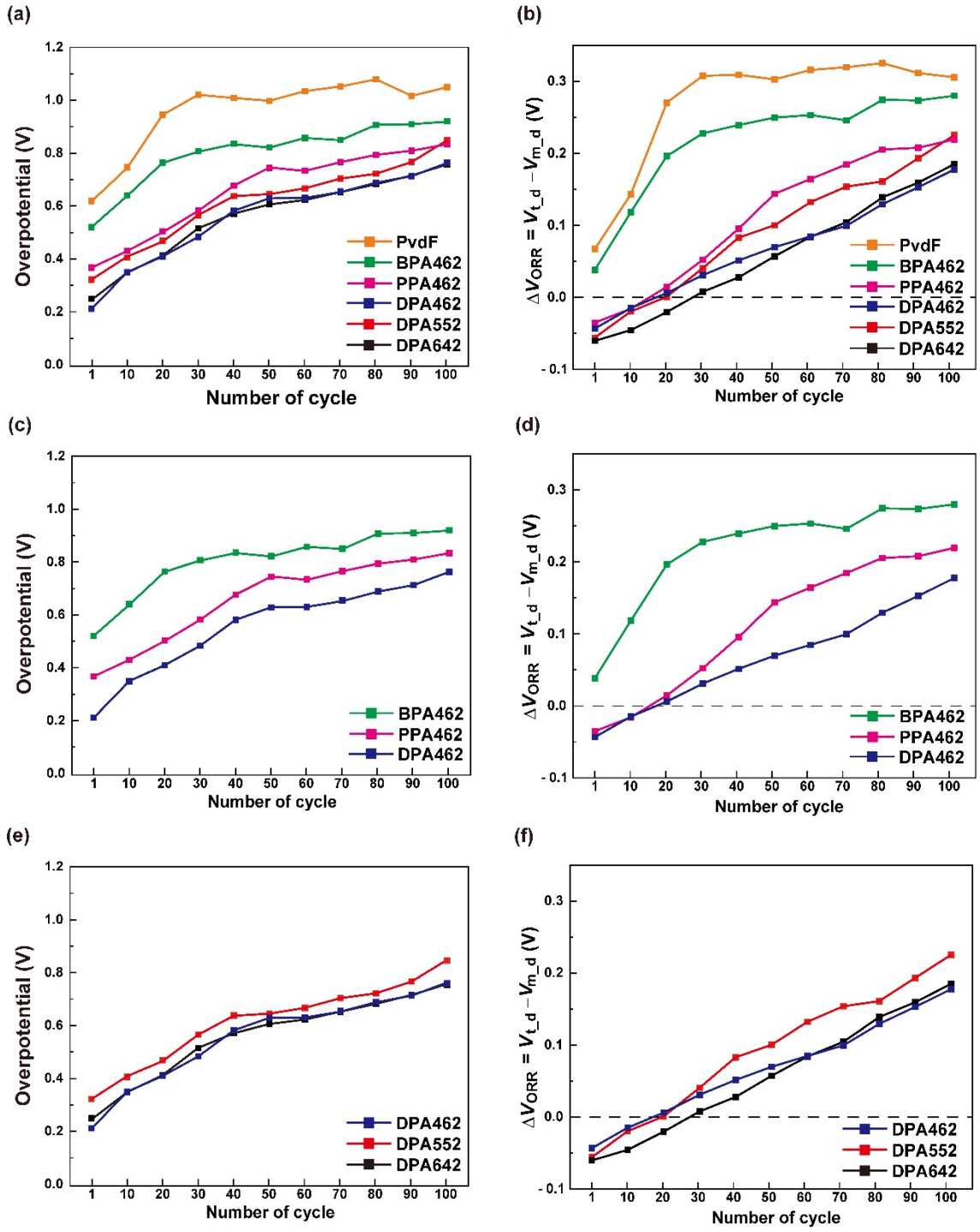

Fig. S18 Overpotential of cells containing polymer binders in (a), (c) and (e) the charge/discharge process and (b), (d) and (f) ORR performance from the theoretical value are plotted as the cycle increases. (a) and (b) show the electrochemical performances of all tested binders. (c) and (d) represent the effects of OH groups at benzene ring structure in binder to electrochemical performances. (e) and (f) show the electrochemical performances according to contents of catechol moiety.

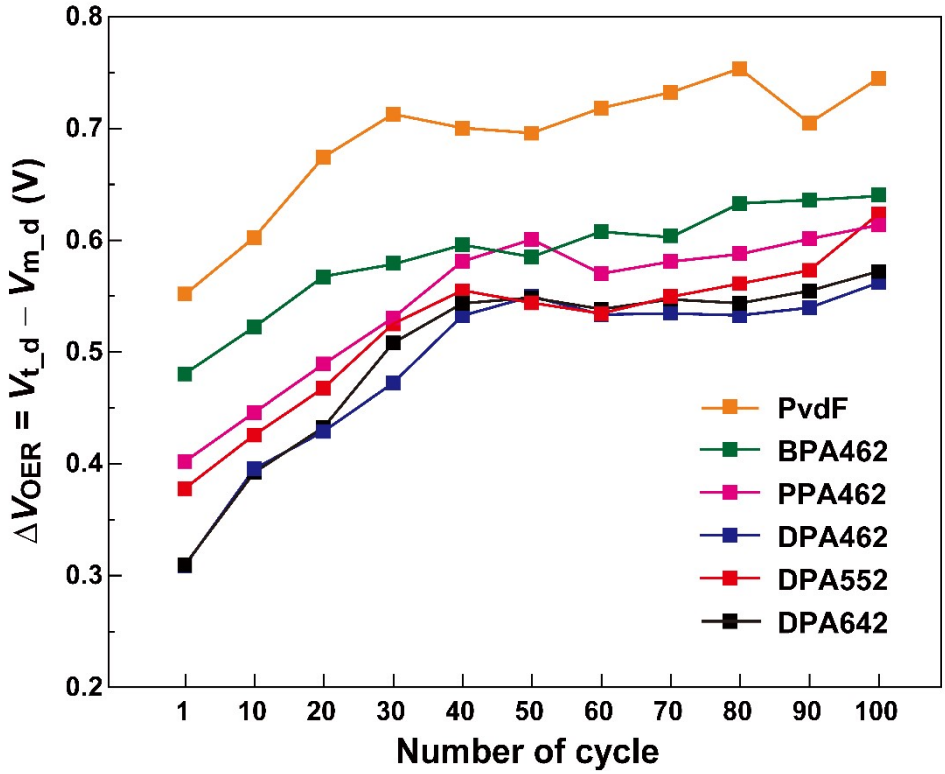

Fig. S19 OER performances of cells containing polymer binders are plotted as the cycle increases.

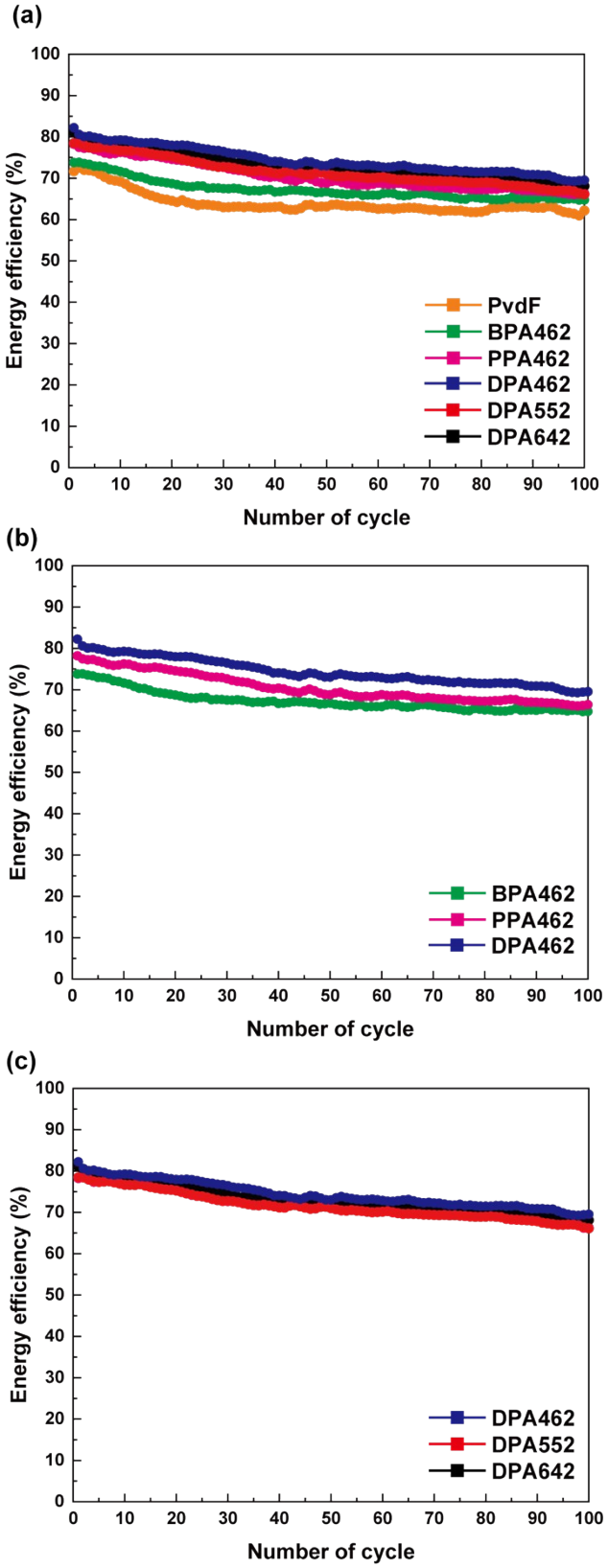

Fig. S20 Energy efficiencies of cells containing polymer binders with increasing cycles. (a) The whole polymer binders. (b) The effect of OH groups at benzene ring in polymer binder structure to energy efficiencies. (c) The energy efficiencies with PEG contents in binder.

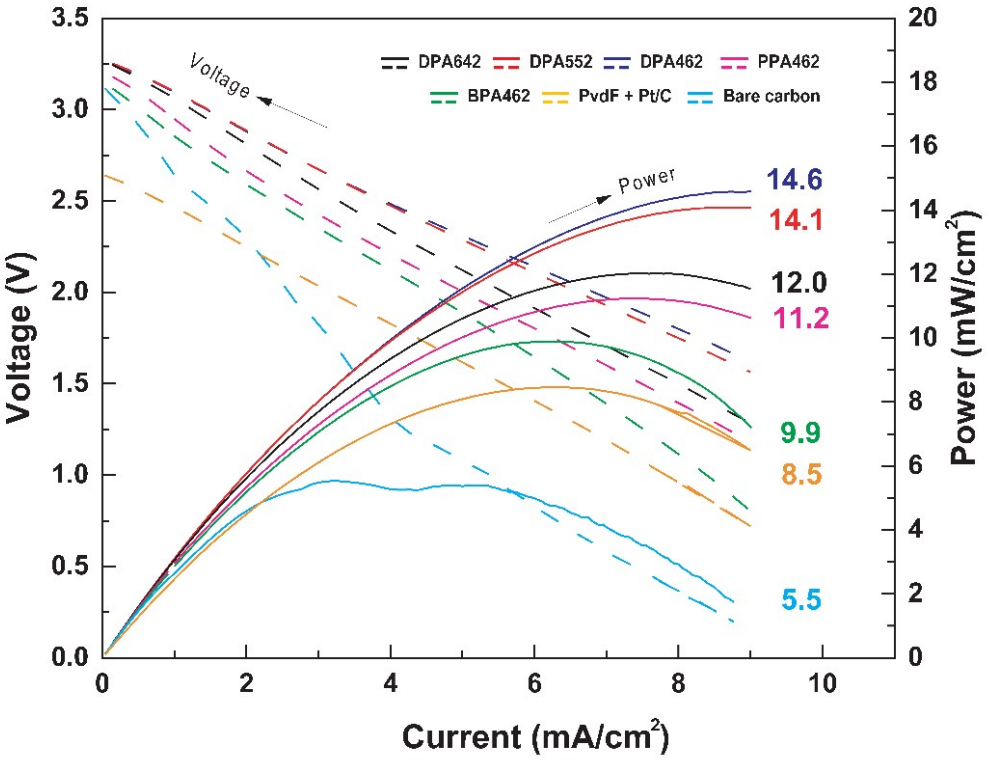

Fig. S21 Polarization and power density curves of synthesized polymer binders and PvdF.

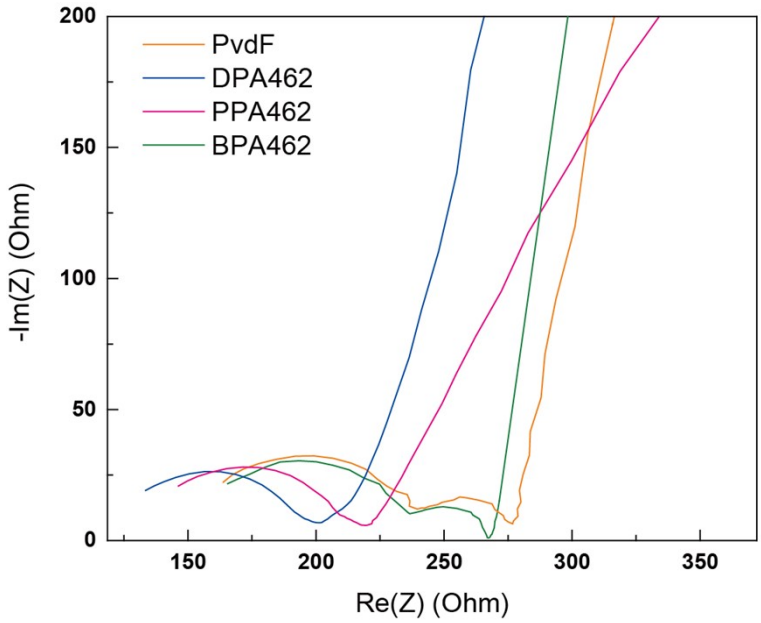

Fig. S22 EIS spectra of DPA462, PPA462, BPA462, and PvdF.

Table S4. Simulated results for the elements of equivalent circuit (Fig. 4(g)).

Sample	R_e (Ω)	R_i (Ω)	R_f (Ω)	R_{ct} (Ω)
DPA462	127.1	33.88	65.6	15.64
PPA462	128.8	33.17	67.93	21.49
BPA462	128.2	30.5	71.58	32.48
PvdF	125.6	32.41	70.69	49.29

References

1. N. Patil, C. Falentin-Daudre, C. Jerome, C. Detrembleur, *Polymer Chemistry* 2015, **6**, 2919.

2. J. Warnant, J. Garnier, A. van Herk, P.-E. Dufils, J. Vinas, P. Lacroix-Desmazes, *Polymer Chemistry* 2013, **4**, 5656.

3. J. Gu, Y. Xiao, N. Dai, X. Zhang, Q. Ni, J. Zhang. Corros. Eng. Sci. Technol., 2019, 54, 249.

4. I. T. McCrum, M. A. Hickner, M. J. Janik, *Langmuir* 2017, **33**, 7043.

5. N. E. Singh-Miller, N. Marzari, *Phys. Rev. B* 2009, **80**, 235407.

6. L. Vitos, A. V. Ruban, H. L. Skriver, J. Kollar, *Surface Science* 1998, **411**, 186.

7. Y., Waseda, K. Hirata, M. Ohtani, *High Temp. High Pressures* 1975, **7**, 221.

8. C. K. Chua, M. Pumera, *Chem. Soc. Rev.* 2014, **43**, 291.